Mass Manufactured Glass Substrates Incorporating Prefabricated Electron Transport Layers for Perovskite Solar Cells

Benjamin Smith[1]*, Joel Troughton[1], Anthony Lewis[1], James McGettrick[1], Adam Pockett[1], Matthew Carnie[1], Cecile Charbonneau[1], Cameron Pleydell-Pearce[1], Justin Searle[1], Paul Warren[2], Su Varma[2] and Trystan Watson[1]†

[1]SPECIFIC, Swansea University, Swansea University, Materials Research Centre, College of Engineering, Bay Campus, Swansea, SA1 8EN, United Kingdom
[2]NSG Pilkington, Pilkington Technology Centre, Hall Lane, Lathom, Ormskirk L40 5UF

Abstract

We present a commercially available glass substrate which incorporates both a FTO and compact TiO_2 layer deposited through CVD that is commonly used in "solar control products". The substrate, known commercially as Pilkington Eclipse Advantage^{TM}, has been designed for use as an infrared radiation control product and this is the first known instance of it being employed and extensively characterized for use as a mass manufactured n-type contact in perovskite solar cells. Using this substrate with no additional compact TiO_2 layer, perovskite solar cells with PCEs of up to 15.9% were achieved. These devices were superior in performance to those where the compact TiO_2 was deposited via spray pyrolysis. The reproducibility and large scale manufacturing base already established with this substrate represents significant potential for solving the problem of upscaling a uniform and pinhole free n-type compact TiO_2 blocking layer.

Key words: Perovskite, Engineering, Science, Materials

1 Introduction

Perovskite solar cells (PSCs) have seen a meteoric rise in prominence amongst the photovoltaic community with power conversion efficiencies increasing from 3.8% in 2009, [1]to over 22% in 2017. [2] [3] [4] With improvements in stability and performance being reported regularly, PSCs appear a promising candidate to compete with existing silicon and thin-film based technologies. The cost associated with organic-inorganic perovskite materials and the technologies to process them is projected to be relatively

*E-mail: 631780@swansea.ac.uk
†E-mail: T.M.Watson@swanseaa.c.uk

low. [5] One of the challenges facing PSCs and other emerging thin film photovoltaics is the scaling up of lab-scale devices to commercial production using inexpensive roll-to-roll or sheet-to-sheet manufacturing techniques. Recently, an article by Youn-Jung Heo and co-workers has demonstrated a fully printed PSC fabricated through the use of slot die coating with a PCE of 14.4%. [6] [7] [8] [9] With these large scale-compatible deposition methods, coupled with novel fast processing techniques, [10] [11] [12] [13] the future looks bright for scaled production of PSCs. PSCs are typically fabricated by solution processing layers onto transparent conducting oxide (TCO)-coated glass. Common TCOs used include fluorine-doped tin oxide (FTO) and tin-doped indium oxide (ITO): FTO-coated glass, in particular, is already produced inexpensively on industrial scales using a chemical vapor deposition technique integrated within the glass production process. Depending on the architecture of the PSC, either a p-type (in the case of "inverted"-type devices) or n-type (in the case of "normal"-type devices) semiconducting layer is deposited onto the TCO-coated substrate. Currently, the majority of "normal" structure devices report TiO_2 as an n-type, electron selective contact; usually in the form of a compact layer followed by a thicker mesoporous layer. [14] [15] The most common reported means of depositing high quality compact layers of TiO_2 at lab scale involve spray pyrolysis of a metal-organic precursor solution. [16] In spray pyrolysis, this solution is sprayed onto a heated substrate, typically at temperatures in excess of 300 ºC to remove the carrier solvent as well as organic ligands associated with the precursor. A subsequent annealing step in excess of 450 ºC is also required to sinter and crystallize the amorphous titanium dioxide into a crystalline anatase form. Although the deposition and heating of such a layer may be scaled up, it may be dangerous owing to the presence of flammable solvent vapor in close contact with heated substrates, as well as being difficult to replicate consistently. This poses a potentially significant bottleneck to the realization of mass-produced perovskite photovoltaics. In this report, we demonstrate efficient PSCs fabricated on a commercially available glass substrate known as "Pilkington Eclipse ^{TM} Advantage" (EA) that is commonly used in solar control products. EA is produced by the glass conglomerate NSG Pilkington and consists of 1.9 mm thick glass with a base layer of 25 nm SnO_2 followed by another 25 nm of SiO_2. On top of this base layer is a 200-250 nm thick FTO layer subsequently overlaid with a 20-40 nm thick TiO_2 layer via CVD (chemical vapor deposition). During standard operation the EA functions as a solar control product allowing the control of heat and light into a building, primarily in warmer climates, where the aforementioned TiO_2 is used to control the optics in the system. EA is manufactured at large scale and is presently commercially available, however although its stack is ordered appropriately and in the correct thickness range for a PSC charge-selective layer, EA has yet to be realized in the use of PSC. In this paper we investigate the potential of using EA as a substrate in perovskite solar cells and characterize its suitability as an electron transport layer (ETL) using techniques including X-ray photoelectron analysis (XPS), Raman spectroscopy, scanning electron microscopy (SEM) and X-ray diffraction analysis (XRD) as well as cyclic voltammetry (CV) and transient photovoltage measurements (TPV).

2 Results and Discussion

During the operation of a PSC, illumination occurs through the glass/ FTO substrate interface thus confirming the importance of optical characterization of these and subsequent layers. Figure 1 shows optical transmission spectra for both EA and a conventional spray pyrolysis processed compact (c)-TiO_2 layer (50 nm) on FTO-coated glass as well as a plain FTO glass (TEC15) sample. In this instance, the sheet resistance of the TCO in both the EA and spray pyrolysis-processed substrate (Solaronix), were measured at 15 Ωsq^{-1} using a Jandel four point probe. It is apparent that both EA and spray pyrolysis processed c-TiO_2 layers on FTO glass exhibit very similar optical transmission between 250 nm and 800 nm. In both cases, the transmission through EA and conventionally coated substrates is markedly reduced compared to FTO glass without a c-TiO_2 layer, especially at shorter wavelengths. Average transmission (AT) values of EA are fractionally lower than that of conventional spray pyrolysis with an AT of 59.52% compared to 60.85%. There is a small blue shift at the band absorption edge in the EA, this is likely due to the variation in glass substrates. EA consists of 1.9 mm thick glass with a base layer of 25 nm SnO_2 followed by another 25 nm of SiO_2. On top of this base layer is a 200-250 nm thick FTO layer subsequently overlaid with a 20-40 nm thick TiO_2 layer via CVD. The spray pyrolysis sample was produced on TEC15 glass that consists 2.2mm thick glass and an FTO film overlaid with a 40-50 nm of spray pyrolyzed TiO_2. The variation in the two samples is likely due to the nature of the glass substrate and thickness of TiO_2.

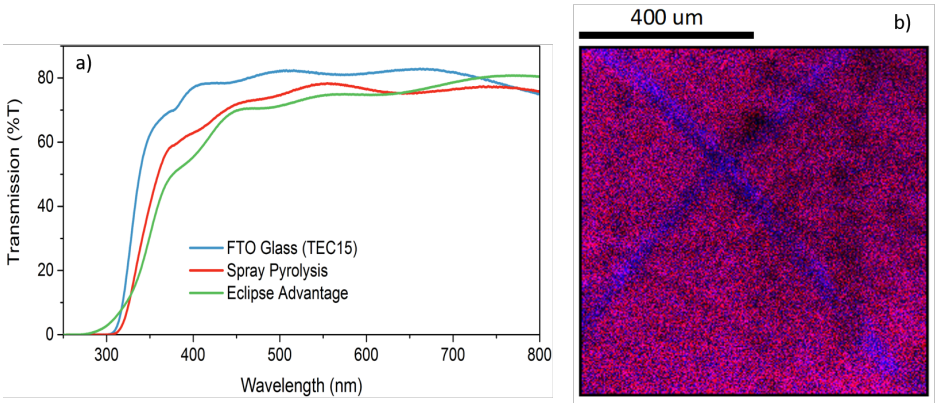

FIGURE 1: (a) UV-visible transmission spectra for Pilkington Eclipse ^{TM}Advantage, as well as conventionally processed c-TiO_2 substrates. Note: Spray pyrolysis indicates FTO (TEC15) with a subsequent application of spray pyrolysed TiO_2. (b) XPS elemental mapping of a scratched Pilkington Eclipse ^{TM} Advantage surface. Red indicates the presence of Ti whereas blue indicates the presence of Sn.

In order to quantitatively determine the surface elemental composition of the TiO_2 layer applied to the EA substrate, x-ray photoelectron spectroscopy (XPS) was employed. Figure 1 shows an elemental map of a mechanically scribed region of the EA in order to expose the underlying surface. A surface layer of Ti is observed (highlighted in red), with exposed Sn (highlighted in blue) seen in the scribed areas, the dark areas are con-

taminants/ debris left over as a result of the scribing process. The analysis showed Ti and O peaks, with the Ti peaks being consistent with Ti (IV) present in TiO_2. With the EA substrate, a significant amount of Sn and C was detected at the surface. These are a result of sample contamination during the manufacturing process. In addition, XPS depth profiling revealed that the Ti layer found on EA is thinner than what might be preferred in PSCs according to literature, [17] estimated to be below 20 nm. However, recent work has shown that highly efficient PSCs utilizing ultra-thin TiO_2 electron transport layers in the region of 2 nanometers are possible. [18] It has also been demonstrated that the crystallinity of such thin layers may not be a barrier to solar cell performance, with PCEs of 19.2% achievable on planar heterojunction devices utilizing an atomic layer deposited amorphous TiO_2. [19] It has also been demonstrated that a compact TiO_2 may not be required at all to achieve reasonable PCEs. [20] [21] [22] Raman spectroscopy was used to further identify the presence of TiO_2 and analysis of the resulting spectra was used to identify any crystalline behavior. Sharp intense peaks give an insight into the degree of crystallinity within a film, while broad, less intense peaks are indicative of amorphous materials. A plot of Raman shift intensity for both spray pyrolysis processed c-TiO_2 and EA substrates is shown in Figure 2. Interestingly, while the TiO_2 indicative peak at 145 cm^{-1} is present for the conventionally processed c-TiO_2 layer through spray pyrolysis, no such peak is present in the EA sample. Figure 2 also shows the spectra of a EA sample having undergone an additional heat treatment at 550 ℃ in order to induce a

crystallographic transformation of any TiO_2 present to the anatase polymorph. Despite a drop in Raman shift intensity around 445 cm^{-1} and 575 cm^{-1}, the anticipated TiO_2 peak fails to manifest itself following heat treatment. X-ray diffraction (XRD) was then employed to probe further the presence of crystalline TiO_2 on both EA and spray pyrolysed processed films. Figure 2 shows x-ray diffraction patterns for both samples. The data suggests that the c-TiO_2 in the spray pyrolysed films is crystalline in nature as suggested by the peak around 25.25 degrees which correlates to the anatase TiO_2 (101) atomic planes. The corresponding peak for FTO at 26.5 degrees can be observed in both samples; the intensity and sharpness of both peaks indicate a highly crystalline film, corroborated by the Raman spectra in Figure 2. The c-TiO_2 in EA is either amorphous, crystalline but too thin to detect or characterized with extremely small grain sizes. Raman spectroscopy and XRD are limited in the analysis of very thin films especially where the crystalline range is also very small. Work carried out by Chandiran et al. and Tilley et al. demonstrated that Raman and XRD are known to suggest very thin films of c-TiO_2 are amorphous in nature. [23] [24] Though they are still prone to crystallization to rutile or anatase at elevated temperatures similar to those employed during fabrication, [25] so crystalline behavior of these thin films cannot be ruled out. The presence of TiO_2 proves difficult to identify through x-ray diffraction and Raman spectroscopy as has been shown previously for ultra-thin layers (less than 20 nm). Cyclic voltammetry (CV) is an electrochemical technique that can uncover the characteristic hole-blocking properties of TiO_2 in the EA substrate when present on an FTO surface. Figure 2 shows cyclic voltammograms of different TiO_2 films exposed to a potassium ferro/ ferri cyanide electrolyte couple. In this experiment, the $Fe(CN)_6{}^{3-/4-}$ solution acts as a model redox system in a three-electrode cell, with the TiO_2 coated FTO glass acting as a working electrode. CV

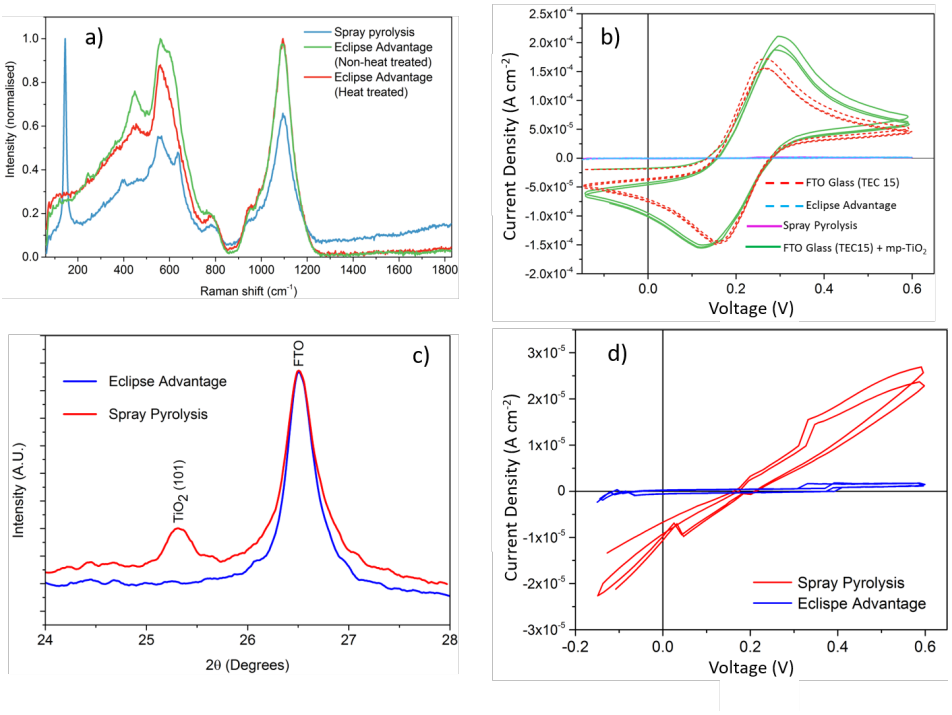

FIGURE 2: (a) Raman spectra measured for a traditional spray pyrolysis processed c-TiO_2 layer of FTO-coated glass, as well as pre and post heat treated Pilkington Eclipse ^{TM} Advantage. (b) Cyclic voltammograms of Pilkington Eclipse ^{TM} Advantage and spray pyrolysis processed c-TiO_2 layers, including additional mesoporous TiO_2 layers.
(c) XRD plot to show the relative peak intensities for Pilkington Eclipse ^{TM} Advantage and Spray Pyrolysis TiO_2 on FTO-coated glass.
(d) Characteristic pinholes found in a spayed compact blocking layer as demonstrated by cyclic voltammetry.

was carried out on several different areas of the eclipse advantage sheets (numerous samples taken from different sheets of 30 cm x 30 cm) supplied by NSG Pilkington to test the effectiveness of the ETL over a large area and compared to similar large area spray pyrolysis device. Each CV measurement was 1 cm x 2 cm.EA and a 50 nm thick spray pyrolysis processed compact TiO_2 layer both show a strong blocking effect over the voltage range as there is minimal current activity, indicating good quality TiO_2 blocking layers with high film coverage that make a rectifying interface. At this point no anodic currents of Ferro cyanide oxidation can flow because TiO_2 is in the depletion regime at these potentials. If the CV scan were to be extended towards -0.7 V the cathodic current will be detected meaning the TiO_2 layer is in the accumulation regime i.e. exhibiting metallic behavior as described by Kavan et al. [26] [27] Pin holes and defects were monitored by measuring any anodic current response; the current measured from these effects arises from the ferrocyanide oxidation at the bare FTO regions, thus indicating an inhomogeneity within the

film. Our results for FTO are within good agreement to that published by Tzu-Sen Su and Kavan et al. [27] [28] One of the major drawbacks to spray pyrolysis has been its relative unreliability to reproduce homogeneous films. The sensitivity of the CV measurement reveals the presence of defects within the c-TiO_2 otherwise undetectable with the naked eye. Characteristic signs of pin holes were deduced from the corresponding increase in anodic activity resulting from ferrocyanide oxidation occurring at uncoated FTO regions as seen in Figure 2. An increase in cathodic activity also indicated relatively poor film coverage for this sample as shown by Tzu-Sen-Su and co-workers. [28] Conversely; EA showed no appearance of defects or pinholes under CV across all samples tested, giving further credence to the reproducible nature of chemical vapor deposition. Bare FTO does not have any hole blocking layer characteristics as evidenced by the Nernstian response in the CV pot in Figure 2. The cathodic (Epc) and anodic peak potential (Epa) are separated by 92.00 mV. The ΔEP is within a reasonable degree to that of the theoretical value of 56.00 mV for a one-electron reversible reaction. This is because of resistances associated with the solution; contacts, area masking, barrier layer lacquer and wiring were not accounted for in these calculations. This means the redox reaction of the electrolyte is electrochemically reversible on bare FTO, suggesting no blocking effect. This result is also within good agreement to that published by Tzu-Sen Su and Kavan et al. [27] [28] The blocking effect of mesoporous TiO_2 scaffolds were also investigated in full devices. 30NRD, procured from Dyesol was prepared by diluting its paste with a mixture of Terpineol and (IPA) to produce a 200 nm thick layer via spin coating. 30NRD has an average nano-particle size of 30 nm, and gives a transparent Titania film with a large surface area to volume ratio upon sintering at 550 °C. The resulting voltammograms in Figure 2 show that a 30NRD mesoporous TiO_2 scaffold exhibits no blocking layer effect, the porous nature of the film allows pinholes to expose bare FTO and so result in a substantial anodic and cathodic current being observed much the same as with bare FTO, again the behavior is Nernstian and the redox reaction reversible. We attribute the very small amount of current (of the order of micro-amperes) observed in the EA and homogeneous spray pyrolysis samples to be down to capacitive charge effects as the number of voltage cycles increases. The small currents detected are a consequence of the lack of Faraday cages used in our set-up which results in small currents being detected from the surrounding environment. [29]

Following confirmation of a blocking function on EA, full devices based on a mixed cation composition were fabricated. The device architecture can be seen in Figure 3, with the perovskite based around published work by Saliba et al. [14] The resulting cesium containing triple cation perovskite of composition $Cs_{0.05}(MA_{0.17}\ FA_{0.83})_{(0.95)}Pb(I_{0.83}\ Br_{0.17})_3$ produces excellent films for power conversion efficiencies as can be seen in Figure 4. We chose to employ the mesoporous scaffold (30RND) into both spray pyrolysis and EA architectures because, to date, cells with the highest overall device efficiencies employ the mesoporous scaffold in their architecture. One key difference in the processing of EA involves the electronic isolation of the cells which is necessary to enable electrode contacting in solar cell fabrication; this is done in spray pyrolysis usually by etching a masked area of FTO with a suitable acid, usually concentrated hydrochloric acid in combination with a reactive metal powder such as Zinc. In order to electrically isolate the

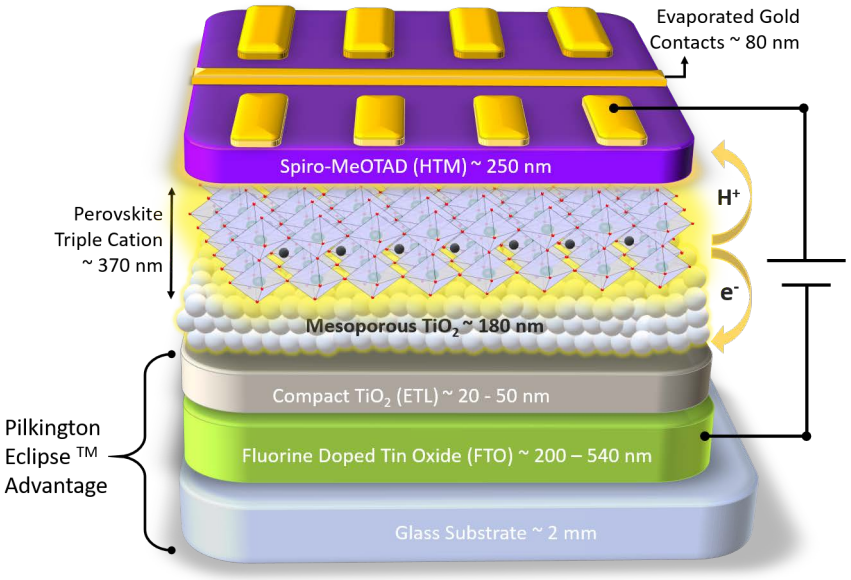

FIGURE 3: Device Architecture of our standard laboratory devices, note perovskite used was the triple cation of composition $Cs_{0.05}(MA_{0.17}\ FA_{0.83})_{(0.95)}Pb(I_{0.83}\ Br_{0.17})_3$.

desired regions of FTO in EA, one must additionally remove the TiO_2 layer that has been chemically vapor deposited on top. We achieved this through the use of a neodymium sourced YVO_4 yttrium orthovanadate laser with wavelength of 532 nm, operating at 32 Amperes. An analysis of Current-Voltage (J-V) statistics for EA devices is presented in Figure 5. Device performance for EA and spray pyrolysis were characterized using a solar simulator (Oriel Sol AAA 940238) and tested under 1 sun illumination in air. It can clearly be seen that EA outperforms spray pyrolysis cells in terms of power conversion efficiencies, the record device for EA achieved a stabilized power conversion efficiency of just under 15% over 180 s of maximum power point tracking (J_{mpp}), the maximum PCE achieved in a single unstabilized device was 15.9% whereas devices with a spray pyrolysis blocking layer achieved a maximum PCE of 14.8% that reduced to 13.1% on stabilized measurement.

The resulting EA JV curve shown in Figure 5 shows there is some residual hysteresis but it appears to be limited and the same can be observed in the spray pyrolysis cells also shown in figure 5,typical of this architecture. The hysteresis in the devices can be attributed to a lack of optimization in the perovskite film processing conditions, such as residual solvents present in our glove box due to a lack of laminar flow capabilities as well as a lack of subsequent treatment of the mesoporous TiO_2 layer such as doping and ozone treatment. It can be seen that the origin of the hysteresis is not due to the TiO_2 ETLs as both TiO_2 ETL deposition methods and devices without a compact ETL show similar levels of hysteresis [30] [31] [32] [33]. The V_{OC} for all devices is relatively high; this would indicate high perovskite film coverage and a low defect density. This is because poor coverage and a high degree of pin holes has been shown to cause a reduction in voltages

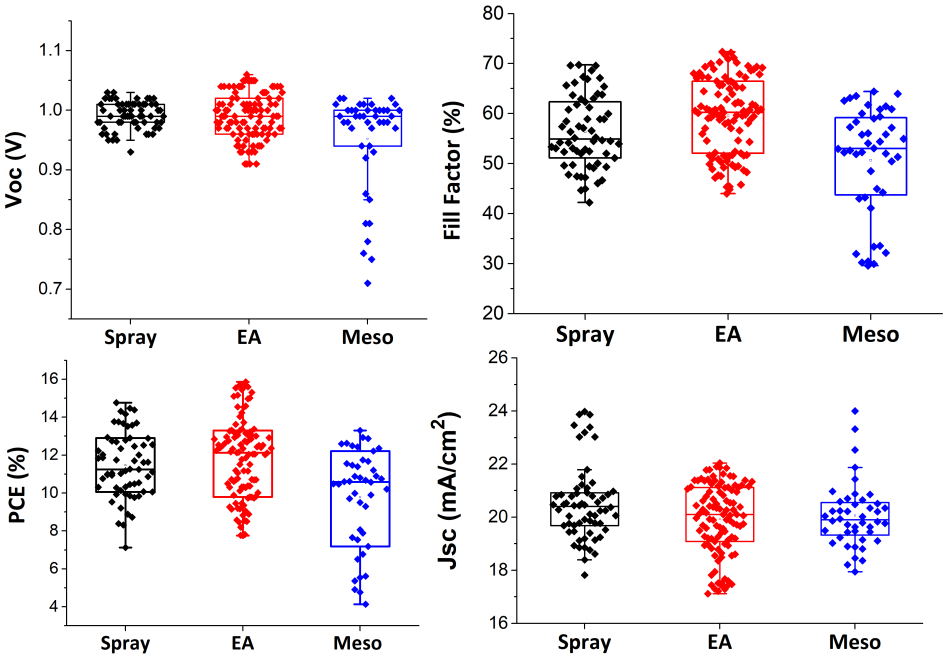

FIGURE 4: Statistical analysis of J-V parameters for spray pyrolysis, Pilkington Eclipse ^{TM} Advantage and samples without a compact TiO_2 layer (labelled Meso). All devices built and tested concurrently to avoid batch to batch variation.

in perovskite devices through recombination at the interface between the compact TiO_2 blocking layers and Spiro-OMeTAD that arises inside pinholes as reported by Carnie et al. [34] The high associated J_{SC} would indicate that there is a sufficient capping layer of perovskite above the mesoporous scaffold that allows for large current densities to be generated. The fill factors for all devices could be considered an area for improvement. Though not low, it appears fill factors have been reduced by the effect of increased series resistance. We attribute this to poor contact at the perovskite — Spiro-OMeTAD interface and a lack of optimized Spiro-OMeTAD processing conditions within our labs as reported by Troughton et al. [11] Devices were also fabricated onto FTO (Solaronix TCO15) with no compact TiO_2 blocking layer whatsoever; these cells again incorporated a mesoporous TiO_2 scaffold into the cell architecture. These devices performed higher when scanned from V_{OC} to J_{SC}. Where a peak PCE was observed at 12.9%, but under testing in the forward direction (J_{SC} to $V_{OC)}$ PCEs reduced to nearly half that when tested in the reverse scan (V_{OC} to $J_{SC)}$. In addition to this, stabilized PCEs were noticeably lower than both spray pyrolysis and EA with a maximum stabilized PCE of 10.7% achieved indicating hysteresis within the cell.

We attribute this to increased recombination of electron-hole pairs due to the lack of blocking effect and subsequent charge separation at the FTO/ Mesoporous TiO_2 / perovskite interfaces within the device. Perovskite film morphology could be further optimized on the EA substrate (for example by varying the deposition process of perovskite)

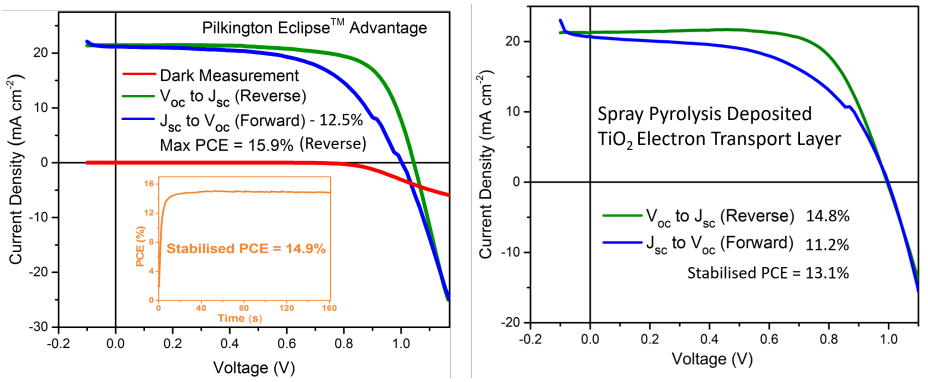

FIGURE 5: JV curves for Pilkington Eclipse ^{TM} Advantage and Spray Pyrolysis deposited TiO_2 showing forward, reverse, dark and stabilized measurements where relevant.

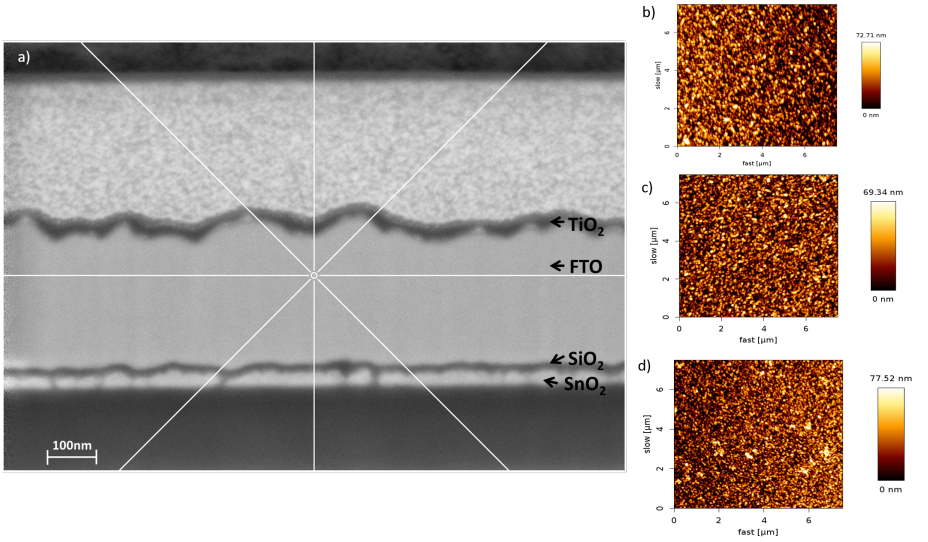

FIGURE 6: (a)Cross sectional SEM of Pilkington Eclipse ^{TM} Advantage taken using a Zeiss Cross beam 540 ultra-high resolution FEG SEM FIB. (b) AFM in contact mode of Solaronix (TEC15) FTO glass
(c) AFM in contact mode of Solaronix (TEC15) FTO overlaid with 50 nm of spray pyrolysis deposited TiO_2.
(d) AFM in contact mode of Pilkington Eclipse ^{TM} Advantage.
All AFM imagery taken using a JPK Nanowizard 3 AFM, using a 0.8 newton meter tip in contact mode. All images taken are of dimensions 7.5 μm by 7.5 μm for comparative purposes.

TABLE 1
Summary for the best performing devices for Pilkington Eclipse^{TM} Advantage, Spray Pyrolysis deposited TiO_2 blocking layers (SP BL) and a blocking layer free device (Meso).

Cell Variant:	Voc (mV)	Jsc ($mAcm^{-2}$)	Fill Factor (%)	Max PCE (%)	Max PCE (stabilized) (%)
EA (Reverse)	1040	21.4	71.2	15.9	14.9
EA (Forward)	1000	21.2	59.3	12.5	
Spray (Reverse)	990	21.3	69.7	14.8	13.1
Spray (Forward)	990	20.7	54.7	11.2	
Meso (Reverse)	980	20.5	64.4	12.9	10.7
Meso (Forward)	1000	19.5	48.5	9.5	

to improve performance as processing conditions for both planar TiO_2 and mesoporous TiO_2 devices is critical [35]. In this study EA still outperforms our optimized spray pyrolysis samples, the mesoporous TiO_2 layer has been optimized for use with spray pyrolysis and not EA. Given the resulting Jsc for both EA and Spray pyrolysis are very similar (21.4 and 21.3 $mAcm^{-2}$ respectively) and the much higher Voc in EA compared to spray pyrolysis in our labs (1040mV and 990 mV) this demonstrates that the perovskite microstructure is not hampered by the EA but rather charge extraction is enhanced and recombination pathways mitigated.Cross sectional SEM images taken using a Zeiss Cross beam 540 ultra-high resolution FEG SEM FIB of EA and Atomic Force Microscopy (AFM) imagery taken using a JPK Nanowizard 3 AFM, using a 0.8 newton meter tip in contact mode can also be seen in Figure 6. The observations confirm that the EA sample has a very thin but highly conformal and homogeneous layer of TiO_2 overlaid upon the relatively large FTO grains. Cross-sectional SEM measurements confirm that the TiO_2 layer is around 20 nm thick as suggested by XPS. The lack of pinholes observed confirms result collected via cyclic voltammetry and XPS, suggesting EA has a very high degree of surface coverage over a large area. The average roughness values (ARV) calculated via AFM analysis show very little difference in EA, Spray pyrolysis and bare FTO glass with ARVs of 14.03, 12.57 and 13.15 nm respectively. The difference in the values is down to natural variation in roughness seen in the FTO. Further analysis on the devices was carried out using steady state and transient photo-voltage measurements to understand the effect of blocking layer quality on recombination. The light intensity dependence of the open circuit voltage, as seen in Figure 7 demonstrates the similarities between the two types of cell employing a blocking layer. Both the spray pyrolysis TiO_2 and EA devices have a similar dependence over two decades of light intensity. The mesoporous-only cell without a blocking layer exhibits a similar trend at high light intensity, with the voltage dropping off sharply below 10% intensity. This suggests that a different recombination process dominates at low light intensity when the cell has no blocking layer. This affect appears to be similar to the case for Dye Sensitized Solar Cells (DSSC) at low intensity without a blocking layer. In DSSC and PSCs this is attributed to recombination processes including the back reaction of electrons via the substrate to the oxidized electrolyte species, [36] or recombination via trap states in the TiO_2 bandgap. [37] The impact of blocking layers

on PSC device performance at low intensity has not been extensively studied, but it is possible that there could be a similar DSSC-like behavior. Gouda et al. [38] have also observed several distinct regions in the trend of open-circuit voltage on light intensity and showed that the electron selective interface has a strong influence upon it. It has also been shown that the underlying TiO_2 blocking layer is more influential than the type of mesoporous oxide used. [10] Recombination processes have been shown to be affected by ion migration and the associated build-up of charged species at the interfaces of the device. [39] [40] [41] [42] It is possible that without the presence of a blocking layer this accumulation of ions is unable to sustain a stable layer and therefore causes a less favorable band structure at the interface resulting in higher recombination. This instability may also be evidenced by the variation in open-circuit voltage at low intensity where a smooth trend is not observed. Further analysis is beyond the scope of this work, but it is clear that a good quality blocking layer is needed to produce cells that will work efficiently over a wide range of light intensities. The transient photovoltage decays displayed simple mono-exponential behavior at all light intensities for the cells containing a blocking layer. At lower intensities the decay transients for the cell without a blocking layer showed double exponential characteristics, similar to previous work considering modifications to reduce interfacial recombination. [36] Again this data shows the almost identical performance of the two blocking layers. The increased rate of recombination at low light intensity for the cell without a blocking layer is evidenced by the sudden tailing-off of the lifetime below 0.9 V as seen in Figure 7.

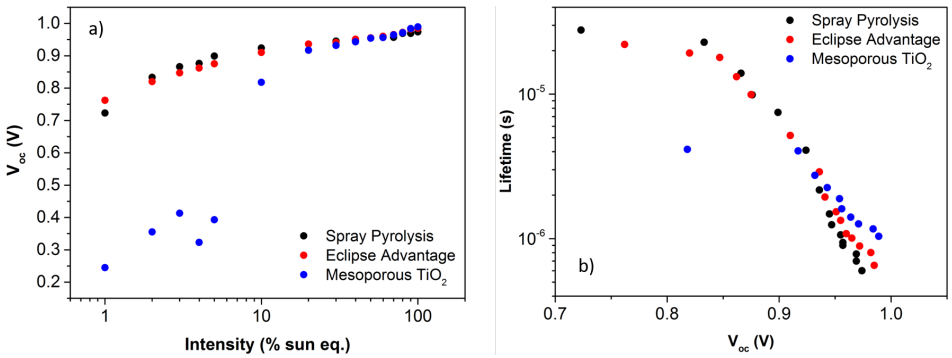

FIGURE 7: (a) V_{OC} verses Intensity measurements of Pilkington Eclipse ^{TM} Advantage, conventional spray blocking layers and Mesoporous TiO_2 . (b) Lifetime verses Voc measurements of Pilkington Eclipse ^{TM} Advantage, conventional spray blocking layers and Mesoporous TiO_2.

At low light intensity the V_{OC} could be reduced by recombination involving trap states in the TiO_2, shunting via the substrate or band edge changes due to ionic migration that are somehow mitigated by the presence of a blocking layer. The emergence of multiple recombination processes at low intensity in the blocking layer free cell is suggested by the transition to double exponential decays. The cells with a blocking layer EA and spray pyrolysis once again show near identical characteristics in open-circuit photovoltage decay (OCVD) measurements, as seen in Figure 8. These cells exhibit a slow decay in V_{OC},

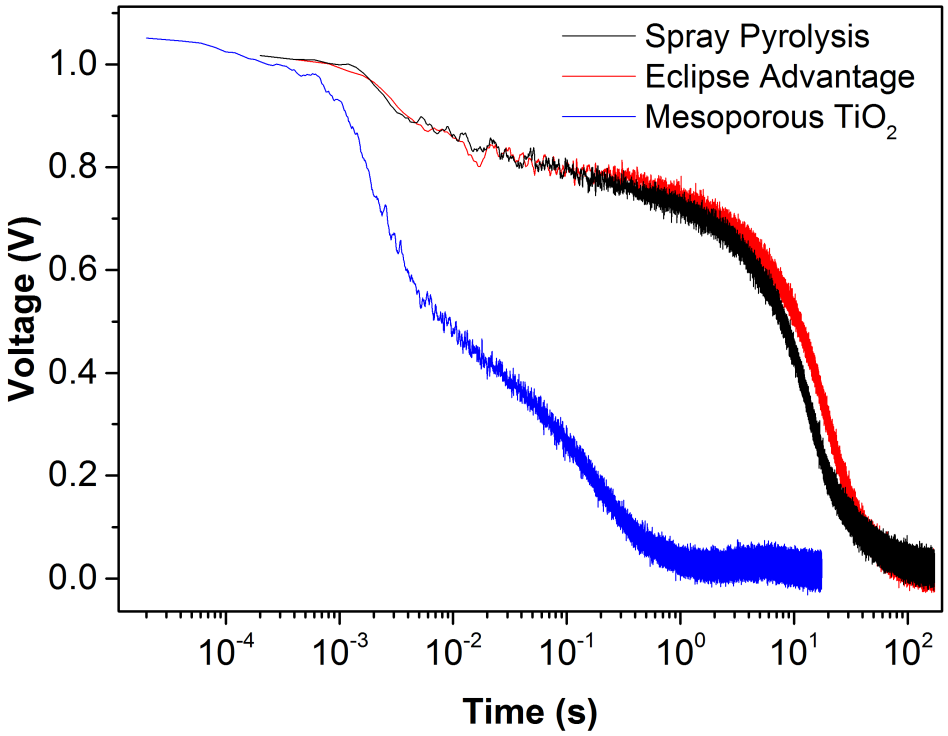

FIGURE 8: Open-circuit photovoltage decay measurements of Pilkington Eclipse ^{TM} Advantage, conventional spray blocking layers and Mesoporous TiO_2.

taking over 1 minute to decay to zero. In contrast, the absence of a blocking layer causes the V_{OC} to decay completely in around 1 s. This striking difference in OCVD behavior has been reported previously in cells that are seemingly identical at 1 sun intensities. [43] The results here suggest that the blocking layer is highly influential for the V_{OC} decay, so this technique may be very useful in analyzing the quality and reproducibility of these layers.

3 Conclusions

The work here presents an alternative technology to depositing compact TiO_2 spray pyrolysis blocking layers. EA originally designed for use as a solar control product, utilizes a thin, < 20 nm CVD TiO_2 compact blocking layer and conductive FTO base layer to perform remarkably well in a mesoporous triple cation perovskite device with PCE exceeding 15%, this is higher than that produced via spray pyrolysis within our research group. XRD, XPS and Raman spectroscopy confirm that the layer of TiO_2 in EA is very thin (<20 nm). The crystalline nature of the TiO_2 proved difficult to surmise owing to the thin nature of the film and the aforementioned limitations of techniques used, however processing conditions under CVD suggest it is crystalline in nature. Despite being designed as a solar control product, EA makes a highly suitable, mass manufacturable perovskite photo-

voltaic substrate, performing well under standard testing conditions, with relatively high short circuit currents, open current voltages and fill factors. There is potential for even better performances by tuning the physical and optical TiO_2 parameters. The substrate has the potential to remove process bottlenecks such as the laborious spraying and sintering of blocking layers while at the same time streamlining the fabrication process to reduce total build times. The use of cyclic voltammetry indicated EA shows a strong blocking effect similar to that found in spray pyrolysis TiO_2 layers sintered at 550°C. TPV and CV analysis shows TiO_2 films on the EA substrate have fewer pinholes and stronger rectifying behavior compared to conventionally processed c-TiO_2 layers prepared via spray pyrolysis. EA doesn't suffer with the inconsistencies and technical difficulties associated with the scaling-up of spray pyrolysis (principally glass cracking and inhomogeneity of film coverage etc.) found when trying to replicate spray pyrolysis at scale. In summary EA proves superior to spray pyrolysis for the large scale production of effective electron transport layers based on TiO_2.

4 Experimental

4.1 Perovskite Solar Cell Fabrication

Pilkington TEC15 TM (<15 Ωcm^{-2}) glass and Pilkington Eclipse TM Advantage were submerged in de-ionised water (<18 mΩ) at 80 ºC for 20 minutes and subsequently rinsed with de-ionised water, acetone, ethanol and isopropanol. The substrates were then blown dry with a nitrogen air knife and placed into an oxygen plasma cleaner for 10 minutes to remove any residual carbon contaminants and make the surfaces more hydrophilic. Electron transport layers (ETL) (where used) were prepared by diluting a solution of 0.2 M titanium di-isopropoxide bis(acetylacetonate) (or TAA) in ethanol and filtered with a 0.2 µm PTFE filter. The deposition of these layers was achieved via manual spraying with an art spray gun (Sealey, Model No. AB932) over the conductive surface of a fluorine-doped tin oxide (FTO)-coated glass. The substrate was pre-heated and maintained at 300 ºC on a hotplate during spraying and a subsequent annealing stage at 550 ºC was carried out for 30 minutes to crystallise the TiO_2 to the anatase phase. A series of 25 sprays were applied successively at 5 s intervals to build up a layer thickness of 40 nm. The mesoporous TiO_2 scaffold was fabricated by diluting a TiO_2 paste, 30-NRD, procured from Greatcell Solar, in a mixture of isopropanol and terpineol (Ratio 30-NRD: terpineol: isopropanol 2:6:4.5 by weight) to produce a 200 nm thick layer via solution processed spin coating (6000 rpm, 2000 $rpms^{-1}$, 30 s). The triple cation perovskite film was fabricated according to the procedures in the literature.[12] The desired triple cation composition consisted of a 5% addition of CsI solution (1.5 M stock solution in DMSO) dispersed in a 95% mixed perovskite precursor to obtain the final composition, $Cs_{0.05}(MA_{0.17}\ FA_{0.83})_{(0.95)}Pb(I_{0.83}\ Br_{0.17})_3$. The solution was then filtered using a 0.2 µm PTFE filter and deposited on top of the mesoporous TiO_2 scaffold via solution processed spin coating (150 µL, 1000 rpm/ 1000 $rpms^{-1}$ for 10 s followed immediately by a 4000 rpm/ 4000 $rpms^{-1}$ for 20 s). During the spin coating process, 150 µL of chlorobenzene was deposited dynamically onto the spinning substrate 10 s before the end

the second spin programme. Upon addition of the anti-solvent (chlorobenzene) the perovskite film immediately turned dark and once the spin coating procedure had finished the films were transferred to a hotplate and annealed at 100 ºC for 1 hour. The entire perovskite procedure was carried out in nitrogen filled glove-box. For the hole transporting material (HTM), a spiro-OMeTAD solution (90 mg of spiro-OMeTAD, 34 µL of 4-tert-butylpyridine (tBP), 19 µL of a lithium-bis(tri-fluoromethanesulfonyl)imide (Li-TFSI) solution (520 mg Li-TFSI in 1 mL acetonitrile) and 10 µL of a FK209 (300 mg in 1 mL of acetonitrile) in 1 mL of chlorobenzene) was spin-coated at 4000 rpm, 2000 rpms^{-1} for 20 s on top of the annealed perovskite. Again the preparation and deposition of the HTM was performed in a nitrogen filled glove-box. Finally 70-80 nm of gold top electrode was thermally evaporated under high vacuum.

4.2 Thin Film Characterisation

Scanning electron Microscopy (SEM) was performed on a Zeiss Crossbeam 540-47-51 ultra-high resolution FEG SEM FIB using a focused ion beam (FIB) probe (30kV:50p) with a working distance of approximately 5.1 mm. X-Ray Photoelectron Spectroscopy (XPS) was carried out using a Kratos Axis Supra (Kratos Analytical) using a monochromated Al Kα source. All data was analyzed on CasaXPS (2.3.17dev6.4k) using the Kratos sensitivity factor library. UV-Vis-NIR spectroscopy was carried out using a Perkin Elmer UV/VIS/NIR spectrophotometer Lambda 750 with a 100 mm InGaAs integrating sphere. Scans from 800-250 nm were taken with a 1 nm data interval at 266.75 nm/ min with transmission mode. Cyclic voltammetry (CV) was conducted using a potassium ferro/ ferri cyanide electrolyte couple. In the experiment, the $Fe(CN)_6{}^{3-/4-}$ solution acts as a model redox system in a three-electrode cell, with the TiO_2 coated FTO glass acting as a working electrode and a calomel electrode acting as a reference electrode. The crystalline properties of the samples were determined by glancing angle X-ray diffraction crystallography (XRD) measurements taken with a D8 Discover instrument from Bruker (Germany) with a CuKα beam at 40 kV, 40 mA and scan parameters of 0.1 s per step at 0.01 2θ step size. (Radiation λ = 1.5406 Å). Raman spectroscopy measurements were taken using a Renishaw Invia Raman microscope. (Operating power: 30mW, Objective lens 50 x magnifications with a 1 µm spot-size, working wavelength 532 nm). All Atomic Force Microscopy (AFM) was imagery taken using a JPK Nanowizard 3 AFM, using a 0.8 newton meter tip in contact mode. All images are of dimensions 7.5 μm by 7.5 μm for comparative purposes.

4.3 Device Characterisation

For current-voltage measurements of solar cells, devices were masked to 0.1 cm 2 and tested under a class AAA solar simulator (Newport Oriel Sol3A) at AM1.5 and 100 mWcm^{-2} illumination conditions calibrated against a KG5 filtered silicon reference cell (Newport Oriel 91150-KG5) using a Keithley 2400 source meter. Current-voltage sweeps were performed from both V_{OC} to J_{SC} and vice versa at a rate of 0.1 Vs^{-1}. For stabilized power output measurements, device bias was set to the maximum power point voltage determined by the J-V sweep and current monitored under 100 mWcm^{-2} illumination. External quantum efficiency measurements were performed in 10 nm increments on a PV Measurements QEX10 in DC mode calibrated against a NIST-traceable photodiode. Transient photovoltage measurements were performed using a commercially

available transient measurement system (Automatic Research GmbH). This system uses a 635 nm red laser diode driven by a waveform generator (Keysight 33500B). The laser pulse length was 10 µs. Background illumination was provided by a white LED with its intensity calibrated to generate the same device photocurrent as measured using the solar simulator. This intensity is referred to as 1 Sun equivalent. Transient responses were captured by a digital storage oscilloscope (Keysight DSOX2024A), the number of sample averages being adjusted to optimize signal noise and measurement time. The device under test is assumed to be held at open-circuit by the 1 MΩ oscilloscope input. Transient photo voltage (TPV) decays were fitted using a single exponential function. Open-circuit photovoltage decay (OCVD) measurements were performed using the same white LED and oscilloscope.

Acknowledgments

The work undertaken here would not have been possible had it not been for the support provided from the Engineering and Physical Sciences Research Council (EPSRC) through the SPECIFIC Innovation and Knowledge center (EP/ N020863/1). The Authors would also like to express their gratitude to the Welsh Government for their support of the Sêr Solar programme. This work has been supported by the European Social Fund (ESF) through the Welsh Government (80339); EPSRC (EP/K503228/1); Swansea University EPSRC impact acceleration account and the COATED doctoral training center, Materials and Manufacturing Centre (M2A), Swansea University College of Engineering. Lastly the authors would like to give special thanks to NSG Pilkington Incubator Projects. A. P. and M. J. C. would like to thank the British Council for funding, through the Newton Al-Farabi Partnership; and the European Regional Development Fund (ERDF) and the Welsh European Funding Office (WEFO) for funding the 2nd Solar Photovoltaic Academic Research Consortium (SPARC II).

References

[1] Kojima, A., Teshima, K., and Miyasaka, Y.S.T. Organometal Halide Perovskites as Visible-Light Sensitizers for Photovoltaic Cells. *Journal of the American Chemical Society*, **2009** (131), 6050–6051.

[2] Shin, S.S., Yeom, E.J., Yang, W.S., Hur, S., Kim, M.G., Im, J., Seo, J., and Seok, J.S.I. (2017) Colloidally Prepared La-Doped BaSnO3 Electrodes for Efficient, Photostable Perovskite Solar Cells. pp. 356–167.

[3] Tobergte, D.R. and Curtis, S. (2013), http://www.nrel.gov/ncpv/images/efficiency_chart.jpg. URL 10.1017/CBO9781107415324.004.

[4] Leijtens, T., Bush, K.A., Prasanna, R., and McGehee, M.D. (2018), Opportunities and challenges for tandem solar cells using metal halide perovskite semiconductors. URL 10.1038/s41560-018-0190-4.

[5] Song, Z., McElvany, C.L., Phillips, A.B., Celik, I., Krantz, P.W., Watthage, S.C., Liyanage, G.K., Apul, D., and Heben, M.J. (2017) A technoeconomic analysis of perovskite solar module manufacturing with low-cost materials and techniques. *Energy & Environmental Science*, **10** (6), 1297–1305. URL 10.1039/C7EE00757D.

[6] Hwang, K., Jung, Y.S., Heo, Y.J., Scholes, F.H., Watkins, S.E., Subbiah, J., Jones, D.J., Kim, D.Y., and Vak, D. (2015) Toward large scale roll-to-roll production of fully printed perovskite solar cells. *Advanced Materials*, **27** (7), 1241–1247. URL 10.1002/adma.201404598.

[7] Hwang, .I. and Yong, K. Novel CdS Hole-Blocking Layer for Photostable Perovskite Solar Cells. *ACS applied materials & interfaces*, **2016** (8), 4226–32.

[8] Heo, Y.J., Kim, J.E., Weerasinghe, H., Angmo, D., Qin, T., Sears, K., Hwang, K., Jung, Y.S., Subbiah, J., Jones, D.J., Gao, M., Kim, D.Y., and Vak, D. (2017) Printing-friendly sequential deposition via intra-additive approach for roll-to-roll process of perovskite solar cells. *Nano Energy*, **41**, 443–451. URL 10.1016/j.nanoen.2017.09.051.

[9] Burkitt, J.S..D. and Watson, T. Perovskite Solar Cells in N-I-P Structure with Four Slot-Die-Coated Layers. *Royal Society Open Science*, **2018** (5), 172 158.

[10] Troughton, J., Bryant, D., Wojciechowski, K., Carnie, M.J., Snaith, H., Worsley, D.A., and Watson, T.M. (2015) Highly efficient, flexible, indium-free perovskite solar cells employing metallic substrates. *J. Mater. Chem. A*, **3** (17), 9141–9145. URL 10.1039/C5TA01755F.

[11] Troughton, J., Carnie, M.J., Davies, M.L., Charbonneau, C., Jewell, E., Worsley, D.A., and Watson, T.M. (2016) Photonic flash-annealing of lead halide perovskite solar cells in 1 ms. *J. Mater. Chem. A*, **4** (9), 3471–3476. URL 10.1039/C5TA09431C.

[12] Carnie, M.J., Charbonneau, C., Davies, M.L., Troughton, J., Watson, T.M., Wojciechowski, K., and Worsley, H.S. (2013) *Lead Iodide Perovskite Sensitized All-Solid-State Submicron Thin Film Mesoscopic Solar Cell with*, Cambridge, England.

[13] Hou, J., Chen, H.Y., Zhang, S., Chen, R.I., Yang, Y., Wu, Y., and Li, G. (2009) Synthesis of a low band gap polymer and its application in highly efficient polymer solar cells. *Journal of the American Chemical Society*. URL 10.1021/ja9064975.

[14] Saliba, M., Matsui, T., Seo, J.Y., Domanski, K., Correa-Baena, J.P., Nazeeruddin, M.K., Zakeeruddin, S.M., Tress, W., Abate, A., and Grätzel, A.H.M. (2016) Cesium-Containing Triple Cation Perovskite Solar Cells: Improved Stability. *Reproducibility and High Efficiency, Energy Environ. Sci*, p. 9.

[15] Heo, J.H., Im, S.H., Noh, J.H., Mandal, T.N., Lim, C.S., Chang, J.A., Lee, Y.H., jung Kim, H., Sarkar, A., Nazeeruddin, M.K., Grätzel, M., and Seok, S.I. (2013) Efficient inorganic–organic hybrid heterojunction solar cells containing perovskite

compound and polymeric hole conductors. *Nature Photonics*, **7** (6), 486–491. URL 10.1038/nphoton.2013.80.

[16] Kavan, L. and Grätzel, M. (1995) Highly efficient semiconducting TiO2 photoelectrodes prepared by aerosol pyrolysis. *Electrochimica Acta*, **40** (5), 643–652. URL 10.1016/0013-4686(95)90400-W.

[17] Charbonneau, C., Cameron, P.J., Pockett, A., Lewis, A., Troughton, J.R., Jewell, E., Worsley, D.A., and Watson, T.M. (2016) Solution processing of TiO 2 compact layers for 3rd generation photovoltaics. *Ceramics International*, **42** (10), 11 989–11 997. URL 10.1016/j.ceramint.2016.04.125.

[18] Chandiran, A.K., Yella, A., Mayer, M.T., Gao, P., Nazeeruddin, M.K., and Grätzel, M. (2014) Sub-nanometer conformal TiO2 blocking layer for high efficiency solid-state perovskite absorber solar cells. *Advanced Materials*, **26** (25), 4309–4312. URL 10.1002/adma.201306271.

[19] Yin, X., Battaglia, C., Lin, Y., Chen, K., Hettick, M., Zheng, M., Chen, C.Y., Kiriya, D., and Javey, A. (2014) 19.2% Efficient InP Heterojunction Solar Cell with Electron-Selective TiO 2 Contact. *ACS Photonics*, **1** (12), 1245–1250. URL 10.1021/ph500153c.

[20] Liu, D. and Kelly, J.Y.T.L. Compact Layer Free Perovskite Solar Cells with 13.5% Efficiency. *Journal of the American Chemical Society*, **2014** (136), 17 116–22.

[21] Wang, J.T.W., Ball, J.M., Barea, E.M., Abate, A., Alexander-Webber, J.A., Huang, J., Saliba, M., Mora-Sero, I., Bisquert, J., Snaith, H.J., and Nicholas, R.J. (2014) Low-Temperature Processed Electron Collection Layers of Graphene/TiO 2 Nanocomposites in Thin Film Perovskite Solar Cells. *Nano Letters*, **14** (2), 724–730. URL 10.1021/nl403997a.

[22] Huang, A., Zhu, J., Zheng, J., Yu, Y., Liu, Y., Yang, S., Bao, S., and Jin, L.L.P. (2017) *Room-Temperature Processible TiO2 Electron Selective Layers with Controllable Crystallinity for High Efficiency Perovskite Photovoltaics*.

[23] Tilley, S.D., Schreier, M., Azevedo, J., Stefik, M., and Graetzel, M. (2014) Ruthenium Oxide Hydrogen Evolution Catalysis on Composite Cuprous Oxide Water-Splitting Photocathodes. *Advanced Functional Materials*, **24** (3), 303–311. URL 10.1002/adfm.201301106.

[24] Chandiran, A.K., Yella, A., Stefik, M., Heiniger, L.P., Comte, P., and Grätzel, M.K.N.M. Low-Temperature Crystalline Titanium Dioxide by Atomic Layer Deposition for Dye-Sensitized Solar Cells. *ACS Applied Materials & Interfaces*, **2013** (5), 3487–3493.

[25] Banfield, J.F., Bischoff, B.L., and a. Anderson, M. (1993) TiO2 accessory minerals: coarsening, and transformation kinetics in pure and doped synthetic nanocrystalline materials. *Chemical Geology*, **110** (1-3), 211–231. URL 10.1016/0009-2541(93)90255-H.

[26] Kavan, T.M..L. and Graetzel, M. Electrochemical Characterization of TiO2 Blocking Layers for Dye- Sensitized Solar Cells. *The Journal of Physical Chemistry C*, **2014** (118), 16 408–16 418.

[27] Kavan, L., Zukalova, M., and Havlicek, O.V.D. (2014), Sol-Gel Titanium Dioxide Blocking Layers for Dye-Sensitized Solar Cells: Electrochemical Characterization, ChemPhysChem.

[28] Su, T.S., Hsieh, T.Y., and Wei, C.Y.H.T.C. Electrodeposited Ultrathin TiO2 Blocking Layers for Efficient Perovskite Solar Cells. *Scientific Reports*, **2015** (5), 16 098.

[29] Wiedemann, D.J., Kawagoe, K.T., Kennedy, R.T., Ciolkowski, E.L., and Wightman, R.M. (1991) Strategies for low detection limit measurements with cyclic voltammetry. *Analytical chemistry*, **63** (24), 2965–70. URL 10.1021/ac00024a030.

[30] Saliba, M., Correa-Baena, J.P., Wolff, C.M., Stolterfoht, M., Phung, N., Albrecht, S., Neher, D., and Abate, A. (2018) How to Make over 20% Efficient Perovskite Solar Cells in Regular (n-i-p) and Inverted (p-i-n) Architectures. *Chemistry of Materials*. URL 10.1021/acs.chemmater.8b00136.

[31] Giordano, F., Abate, A., Baena, J.P.C., Saliba, M., Matsui, T., Im, S.H., Zakeeruddin, S.M., Nazeeruddin, M.K., Hagfeldt, A., and Graetzel, M. (2016) Enhanced electronic properties in mesoporous TiO2 via lithium doping for high-efficiency perovskite solar cells. *Nature Communications*. URL 10.1038/ncomms10379.

[32] Abdi-Jalebi, M., Dar, M.I., Sadhanala, A., Senanayak, S.P., Giordano, F., Zakeeruddin, S.M., Grätzel, M., and Friend, R.H. (2016) Impact of a Mesoporous Titania-Perovskite Interface on the Performance of Hybrid Organic-Inorganic Perovskite Solar Cells. *Journal of Physical Chemistry Letters*. URL 10.1021/acs.jpclett.6b01617.

[33] Kim, H.S. and Park, N.G. (2014) Parameters Affecting I-V Hysteresis of CH3NH3PbI3 Perovskite Solar Cells: Effects of Perovskite Crystal Size and Mesoporous TiO2 Layer. *The journal of physical chemistry letters*, **5** (17), 2927–34. URL 10.1021/jz501392m.

[34] Carnie, M.J., Charbonneau, C., Davies, M.L., Regan, B.O., Worsley, D.A., and Watson, T.M. (2014) Performance enhancement of solution processed perovskite solar cells incorporating functionalized silica nanoparticles. *J. Mater. Chem. A*, **2** (40), 17 077–17 084. URL 10.1039/C4TA03387F.

[35] Eperon, G.E., Burlakov, V.M., Docampo, P., Goriely, A., and Snaith, H.J. (2014) Morphological control for high performance, solution-processed planar heterojunction perovskite solar cells. *Advanced Functional Materials*. URL 10.1002/adfm.201302090.

[36] Cameron, L.M.P..P.J. and Hore, S. How Important is the Back Reaction of Electrons via the Substrate in Dye-Sensitized Nanocrystalline Solar Cells? *Journal of Physical Chemistry B*, **2005** (109), 930–936.

[37] Salvador, P., Hidalgo, M.G., and Bisquert, A.Z.J. Illumination Intensity Dependence of the Photovoltage in Nanostructured TiO2 Dye-Sensitized Solar Cells. *Journal of Physical Chemistry B*, **2005**, 109–15 915.

[38] Gouda, L., Gottesman, R., Ginsburg, A., Keller, D.A., Haltzi, E., Hu, J., Tirosh, S., Anderson, A.Y., and Boix, A.Z.P.P. Open Circuit Potential Build-Up in Perovskite Solar Cells from Dark Conditions to 1. *Sun, Journal of Physical Chemistry Letters*, **2015**, 6–4640.

[39] Reenen, M.K..S.V. and Snaith, H.J. Modeling Anomalous Hysteresis in Perovskite Solar Cells. *Journal of Physical Chemistry Letters*, **2015**, 6–3808.

[40] Richardson, G., O'Kane, S.E.J., Niemann, R.G., Peltola, T.A., Foster, J.M., and Walker, P.J.C.A.B. (2016) Can Slow-Moving Ions Explain Hysteresis in the Current–Voltage Curves of perovskite Solar Cells? *Energy Environ. Sci*, pp. 9–1476.

[41] Pockett, A. and Carnie, M.J. (2017) Ionic Influences on Recombination in Perovskite Solar Cells. *ACS Energy Letters*, **2** (7), 1683–1689. URL 10.1021/acsenergylett.7b00490.

[42] Calado, P., Telford, A.M., Bryant, D., Li, X., Nelson, J., O'Regan, B.C., and Barnes, P.R. (2016) Evidence for ion migration in hybrid perovskite solar cells with minimal hysteresis. *Nature Communications*, **7**, 13 831. URL 10.1038/ncomms13831.

[43] Pockett, A., Eperon, G.E., Peltola, T., Snaith, H.J., Walker, A., and Cameron, L.M.P.P.J. Characterization of Planar Lead Halide Perovskite Solar Cells by Impedance Spectroscopy, Open-Circuit Photovoltage Decay, and Intensity-Modulated Photovoltage/Photocurrent Spectroscopy. *The Journal of Physical Chemistry C*, **2015**, 119–3456.